



Collapse of Deep-Sea Circulation during an Eocene Hyperthermal Hothouse – A DeepMIP Study with CESM1.2

Arne M.E. Winguth¹, Mikaela Brown¹, Pincelli Hull², Elizabeth Griffith³, Christine Shields⁴, Ellen Thomas², and Cornelia Winguth¹

5 ¹Department of Earth and Environmental Sciences, University of Texas Arlington, 500 Yates St., Arlington, TX 76016, USA.

²Department of Geology and Geophysics, Yale University, P.O. Box 208109, New Haven, CT 06520-8109, USA.

³School of Earth Sciences, The Ohio State University, South Oval Mall, Columbus, OH 43210, USA.

⁴National Center for Atmospheric Research, P.O. Box 3000, Boulder, CO 80307-3000, USA.

10 *Correspondence to:* Arne M.E. Winguth (awinguth@uta.edu)

Abstract. During the Paleocene-Eocene Thermal Maximum (PETM, ~56 Ma), a rapid injection of greenhouse gases (with isotopically depleted carbon) into the atmosphere led to a ~5 °C global temperature rise, ocean acidification, and perturbation of marine and terrestrial ecosystems. In this study, we carried out a series of DeepMIP climate sensitivity experiments using the Community Earth System Model CESM1.2 to evaluate how changes in the radiative forcing could have contributed to Eocene hyperthermal events. An atmospheric change from 3xCO₂ relative to pre-industrial levels (PAL) equivalent during the latest Paleocene to 6xCO₂ PAL in response to a carbon input pulse of 1680 PgC resulted in equatorial warming to 36.9 °C consistent with proxy estimates. The lower equator-to-pole temperature gradient in this 6xCO₂ PAL scenario as compared to the pre-industrial experiment with 1x CO₂ PAL is due to the lack of an ice sheet, the increase in greenhouse gases, and a lower cloud optical depth. The climate simulations suggest an intensified hydrological cycle with higher precipitation in the tropics, particularly over the Indian Eocene continent, and in mid-latitude. In contrast, mega-droughts are prominent in the subtropics, particularly in Africa and South America. Topographic effects such as the closure of the Drake Passage and the more southern location of Australia as well as a lower-than-present meridional temperature gradient contribute to a much weaker surface ocean circulation near the Antarctic continent, as compared to the current pronounced Antarctic Circumpolar Current. In response to the increase in greenhouse gas forcing to 6xCO₂ PAL, deep water formation in the Southern Ocean nearly collapsed and changed from a southern-dominated deep-sea ventilation to a weak deep water formation in the North Atlantic Ocean and further to a polar collapse of deep water formation and a shallow haline-mode ventilation in the subtropics at 12xCO₂ PAL. Bipolar convective overturning in the Pacific Ocean is not supported and remains uncertain, but southern component water mass formation in the Pacific Ocean has been simulated with 1x CO₂ PAL. Increased stratification and reduced solubility of dissolved oxygen caused by warming may have contributed to lower abyssal dissolved oxygen concentrations and thus stresses on the marine ecosystem. However, decreased upwelling and productivity may have decreased the apparent oxygen utilization and thus could have increased the oxygen concentration in the twilight zone.



1 Introduction

35 The generally warm climate of the early Paleogene (~65-45 Ma) was characterized by multiple, rapid, short-term global warming events, termed “hyperthermals”. Paleogene hyperthermal events were caused by massive greenhouse gas release into the ocean-atmosphere, and impacted the Earth’s ecosystems, biotic evolution, and global carbon cycle. As such, hyperthermals, the most extreme of which was the 5°C - 8°C warming (Dunkley Jones et al., 2013; Lunt et al., 2017) during the Paleocene-Eocene Thermal Maximum (PETM; ~56 Ma; Kennett and Stott, 1991; Westerhold et al., 2011), may be important for understanding ongoing anthropogenic-induced global warming and its long-term effects on the environment.

40 The PETM is recognized as a major global carbon cycle disturbance (DeConto et al., 2012; Dickens, 2011; Thomas and Shackleton, 1996; Röhl et al., 2007, Sluijs et al., 2007, Bowen et al., 2015). Estimates of the total amount of carbon released during the PETM range from 3,000 to 10,000 petagrams (Pg) (e.g., Zachos et al., 2005; Zachos et al., 2008; Bowen et al., 2015), potentially initiated by volcanism from the North Atlantic Igneous Province (Gutjahr et al., 2017), that could have triggered disturbances of surface sedimentary carbon reservoirs, climate-carbon cycle feedbacks, associated widespread ocean acidification (Zachos et al., 2005; Penman et al., 2014), and extinction of deep-sea benthic foraminifera (Thomas, 2007).

45 Past paleoclimate sensitivity studies (Lunt et al., 2012; Lunt et al. 2021; Inglis et al., 2020) generally reproduce PETM tropical warming, a lower pole-to-equator temperature gradient, and reduced poleward heat-transport due to a rise in atmospheric pCO₂ (Winguth et al., 2010). Changes in poleward heat transport have also been attributed to the open central American seaway and the closed Drake passage (e.g. Kenneth, 1973; Mikolajewicz et al. 1996, Sijp et al., 2009, Toumoulin et al., 2020), and open passageways between the Atlantic and Arctic Ocean (Shellito et al., 2009; Winguth et al., 2010). positive feedbacks on high-latitude winter marine climate change involving convective clouds (Abbot et al., 2009), reduced cloud condensation nuclei (CCN) (Kump and Pollard, 1998; Kiehl and Shields, 2013), or a generally warmer climate including hotter tropics (Huber, 2008).

55 In this study, we assess whether increases in atmospheric radiative forcing and associated changes in surface buoyancy forcing are consistent with paleo proxies. Specifically, we focus on the contribution of changes in these forcings to a change in ocean circulation at the onset of the PETM and the comparison of these simulated changes with circulation proxies.

2 Model Description

2.1 Community Earth System Model

60 In this study, the Community Earth System Model version 1.2 (CESM1.2) (Gent et al., 2011; Hurrell et al., 2013) was applied with a horizontal resolution in the atmosphere and land of finite volume ~1.9°x2.5° with 26 layers, and in the ocean a nominal resolution of 1°x1° with 60 vertical layers. Eocene boundary conditions follow the DeepMIP protocol (Lunt et al., 2017) as summarized together with the model description. The model has been integrated for nearly ~ 2000 years to allow adjustment of tracers in the deep sea.



1.2 DeepMIP Boundary and Initial Conditions

65 Boundary conditions for the PETM have been defined in DeepMIP (Lunt et al., 2017; Table 1). Paleo-topographic boundary conditions were modified from Herold et al. (2014) by including a subgrid topographic parameterization, tidal dissipation, river runoff, aerosols, and a land surface distribution to allow throughflow through narrow passages. Solar insolation ($S_0 = 1361$ $W m^{-2}$) and orbital forcing (eccentricity $e = 0.06$ and obliquity $\varepsilon = 23.5^\circ$) are kept at pre-industrial levels for all PETM experiments according to the DeepMIP protocol to allow a suitable comparison of the $1xCO_2$ simulation with the preindustrial
70 experiment. It is assumed that the radiative forcing increase in solar radiation from the early Eocene to pre-industrial levels was compensated by the decrease in radiative forcing by the atmospheric methane concentration at that time.

Four sensitivity experiments with different CO_2 radiative forcings at 1x, 3x, 6x, and 12x preindustrial atmospheric levels (PAL) of 280 ppmv have been conducted according to the DeepMIP protocol (Table 1). In addition, a $1xCO_2$ scenario with pre-industrial (1850) boundary conditions was carried out and compared to the $1xCO_2$ Paleocene Baseline experiment with Eocene
75 topographic and ice sheet boundary conditions. The $3xCO_2$ scenario represents conditions of the latest Paleocene (LP) before the onset of the PETM (or hyperthermal events), whereas the $6xCO_2$ and $12xCO_2$ PAL are carbon pulse sensitivity scenarios as inferred from the carbon isotope excursion (CIE).

Aerosol forcings likely were different than during pre-industrial conditions, thus could play an important role in climate change (see Kump and Pollard, 2008; Kiehl and Shields, 2013). We are using aerosol forcing from Herold et al. (2014) that utilizes
80 output from a Bulk Aerosol Model (Neale et al., 2010) and explicitly simulates the distribution of dust, sea salt, sulphate, and organic and black carbon aerosols consistent to the Eocene topography. The results from the $1xCO_2$ PAL experiment with Eocene aerosol forcing are comparable to an additional sensitivity experiment at $1xCO_2$ PAL with pre-industrial aerosol forcing (and thus not listed in Table 1).

The model has been initialized from a depth(z) and latitude(φ)-dependent temperature profile (with a vertically declining
85 temperature $T = 25^\circ C \cos(\varphi) (6000 z)/6000 + 15^\circ C$ for temperature $z \leq 5000$ m and $15^\circ C$ for $z > 5000$ m) and from a vertically uniform salinity ($S = 34.7$) profile. All experiments have been integrated for 2000 years to near-equilibrium state and the top of the atmosphere energy balance has an absolute value below $0.55 W m^{-2}$ for $1xCO_2$ PAL and below $0.29 W m^{-2}$ for $3xCO_2$ PAL and higher CO_2 values which is slightly above the $0.147 W m^{-2}$ of CCSM4 at FV 0.9×1.25 atmospheric resolution.

3 Results

90 3.1 Simulated Paleocene Climate at $1xCO_2$

Below, the Paleocene baseline scenario at pre-industrial CO_2 radiative forcing was compared to the preindustrial (PI) simulation with the same CO_2 radiative forcing (as part of the DeepMIP protocol) in order to explore the effects of topography, ice sheets, land surface, and aerosol forcing. A detailed summary of this Paleocene baseline simulation is given in Brown (2019). Differences in the global average surface air temperature (SAT) between the scenarios with Paleocene aerosol forcing



95 (1xCO₂ Paleocene Baseline, PB, scenario) and the scenario with 1xCO₂ Paleocene Baseline with preindustrial aerosol forcing (PB_PR scenario) are negligible.

The global average surface air temperature (SAT) is 7.4 °C higher for the 1xCO₂ Paleocene Baseline scenario than for the preindustrial simulations (Table 1; Fig. 1 and Fig. 2). SAT anomalies are amplified in polar regions (~44 °C over Antarctica, ~13 °C over the Arctic Ocean) and are linked to a lack of ice sheets, and surface and cloud albedo feedbacks. The difference
100 in surface elevation over Antarctica between the 1xCO₂ PETM scenario without ice sheets, and the preindustrial scenario exceeds 3km. Such an elevation change may result in ~18°C surface temperature change if a polar lapse rate of ~6 °C/km (as inferred from the 1xCO₂ Paleocene Baseline scenario) is assumed. The higher-than-pre-industrial surface air temperature in the 1xCO₂ Paleocene Baseline experiments leads to a reduced snow height and snow-free areas over West Antarctica, which in turn reduce the reflectivity and amplify the warming. Sea surface air temperatures in the tropics (20°S to 20°N) are ~30.6°C
105 in the 1xCO₂ Paleocene Baseline, 3.7°C warmer than in the preindustrial experiment, linked to a rise in surface temperatures and water vapor concentration in the atmosphere.

Global pole-to-equator precipitation patterns for the 1xCO₂ Paleocene Baseline scenario (Fig. 3 and Fig. 4) are comparable with the present-day, with precipitation higher than evaporation in the tropics and high-latitudes, and evaporation exceeding precipitation in the downward branch of the Hadley circulation cells. Global precipitation is ~18% higher in the 1xCO₂
110 Paleocene Baseline Scenario than in the PI experiment because of an increase in the latent heat flux from the surface to the atmosphere due to warmer polar temperatures, absence of ice sheets, and changes in the land surface albedo and thus enhanced water vapor in the atmosphere. The precipitation increases over land (by ~36%) in the 1xCO₂ experiment relative to the preindustrial conditions is linked to heavy rainfall over the tropics, due to the intensification of moisture transport along the lower branch of the Hadley Cell into the intertropical convergence zone (ITCZ; Fig. 5 and 6; Held and Soden, 2006). In
115 addition, enhanced precipitation is simulated over India (island effect), over northern South America with the opening of the Central American Seaway, and over West Africa due to the presence of an inland sea. Increased precipitation occurs at latitudes greater than 60° supporting a climate feedback associated with the hydrological cycle that may amplify the exceptional polar warmth (Pagani et al., 2006). Land-sea breezes may have influenced coastal wind patterns around Antarctica in this 1xCO₂ Paleocene Baseline scenario. The reduced air-sea temperature difference due to a lack of ice sheets contributed to a reduction
120 of the meridional temperature gradient and near sea ice-free conditions in proximity of Eocene Antarctica.

As a result of the lack of ice sheets and topographic changes, ocean currents around Antarctica in the 1x CO₂ Paleocene Baseline scenario were more sluggish than in the PI simulation. Closed or narrow gateways at the Tasman Sea and Drake Passage and an open Central American Seaway during the early Eocene, together with the reduced wind stress (Fig. 5) and weak meridional temperature gradient contributed to a substantially weaker-than-present ocean circulation, with the maximum
125 transport exceeding 180 Sverdrup (1 Sv = 10⁶ m³ s⁻¹) for the PI experiment as compared to 50 Sv for the 1xCO₂ PETM experiment (Fig. 5).

Compared to pre-industrial conditions, the low meridional temperature gradient and associated reduced wind stress as well as the open Central American Seaway led to weakening of the barotropic stream function in the North Atlantic Current by about



30 Sv (Fig. 5). In the southern hemisphere, the lack of an ice sheet, and thus a substantially weaker-than-preindustrial meridional temperature gradient and associated reduced westerly wind stress, support a relatively slow westward-directed flow of 10 Sv-30 Sv around Antarctica, as compared to the pre-industrial strength of the westerly subpolar current around continental Antarctica, with values reaching nearly 200 Sv. In addition, the closed Drake Passage and Tasman Gateway and/or open Central America Seaway resulted in a relatively sluggish current around Antarctica during the early Eocene (Figure 5a). Reduced equatorward Ekman transport with declined wind stress produced favorable conditions for a deeper-than-preindustrial mixed-layer depth in the proximity of the paleo-Weddell and Ross Sea, a higher-than-pre-industrial stratification in the North Atlantic Ocean (Fig. 6), and a global meridional overturning circulation with a dominant deep southern component and a shallow northern component (Fig. 7), consistent with previous studies (see for example Elsworth et al., 2017; Goldner et al., 2014; Inglis et al., 2015; Lefebvre et al., 2012; Mikolajewicz et al., 1993; Nong et al., 2000; Sijp et al., 2009; Zhang et al., 2010; Toumoulin et al., 2020).

There is almost no seasonal sea ice present around Antarctica in the 1xCO₂ Paleocene Baseline scenario, whereas winter sea ice is simulated in the Arctic Ocean. Low salinity due to the wetter-than-present Arctic conditions and enhanced freshwater input from the adjacent land masses promotes sea ice formation during the boreal winter.

3.2 The 3xCO₂ LP Scenario

The increase in CO₂ radiative forcing from 1xCO₂ to 3xCO₂ PAL leads to a substantial rise in the SAT and sea surface temperature (SST) of 3.8 °C and 3.8 °C, respectively (Table 1). The 3x CO₂ latest Paleocene (LP) experiment simulates a 2.9 °C higher SAT in the tropics (20°N to 20°S) relative to the 1x CO₂ Paleocene baseline scenario, in response to the increase in CO₂ concentration and the associated climate feedbacks (Figs. 1 and 2a). The polar amplification of SAT (with an increase ranging from 8 °C to 13 °C) in the 3x CO₂ latest Paleocene scenario relative to the 1x CO₂ Paleocene reference case is linked to the ice albedo climate feedback. The north polar annual mean SAT in the 3x CO₂ latest Paleocene experiment is above freezing (3°C), whereas SAT near the South Pole is below freezing (-5 °C) due to Antarctic continentality.

Differences in precipitation patterns relative to the 1xCO₂ Paleocene baseline scenario follow future CESM1 climate change scenarios e.g. Meehl et al., 2013 with an increase in precipitation over the intertropical convergence zone, specifically over orographic features such as the Indian microcontinent, Northern Columbia, Western Central Africa, and Southeast Asia, and in subpolar latitudes along the westerly rain belts. High-latitude precipitation increased along mountain ranges on the windward side of the westerly wind zones such as the Canadian Rockies and Patagonian Andes, and the West Antarctic Peninsula. Humid regions are associated with the ITCZ and midlatitude regions whereas arid regions are in proximity of the downward branch of the Hadley circulation. The hydrological cycle is amplified in the 3xCO₂ latest Paleocene experiment compared to the 1xCO₂ Paleocene reference scenario, thus resulting in increased humidity in the tropics, particularly over India, and increased aridity over the subtropics due to an increase in evapotranspiration primarily in the Eastern Tethys region and southwest Africa.

Wind stress and barotropic stream function decreased relative to the 1xCO₂ scenario, linked to polar amplification and a reduced meridional temperature gradient in response to an increase in sea-ice albedo, land snow cover, and associated



feedbacks. Trade winds (Fig. 5) and equatorial Ekman-induced upwelling declined by ~50% (Fig. 8), thus affecting surface temperature (Fig. 2a), net primary, and export production (Winguth et al., 2013).

Enhanced stratification with an increase in the CO₂ radiative forcing in the 3xCO₂ LP scenario as compared to the 1xCO₂ scenario led to a shallower mixed-layer depth layer (Fig. 6) and a weaker global meridional overturning cell, in particular a reduction in the southern component water masses (Fig. 7).

3.3 The 6xCO₂ and 12xCO₂PETM Scenarios

The sea surface temperature of the 6xCO₂ PETM and 12xCO₂ PETM climate simulations is 2.4 °C and 7°C respectively warmer than that of the 3xCO₂ simulation (Table 1). Change in global SAT over land is comparably higher with a 4.3 °C and 10.4 °C respective rise due to multiple factors including polar decline in snow depth liquid water content equivalent, decrease in soil moisture, and associated lower heat capacity of soils and decline in latent heat flux. Changes in the Northern Hemisphere are even higher due to the land distribution, with a temperature increase above 7 °C.

Precipitation patterns in the 6xCO₂ experiment are generally amplified (and even more so in the 12xCO₂ experiment) compared to the 3xCO₂ scenario in tropical and mid-to-high latitudes, because vapor moisture saturation increases ~7% per 1 °C increase based on the Clausius-Clapeyron equation. Relative to the 3xCO₂ scenario, there is a substantial increase in precipitation along the ITCZ, specifically over India and Northern South America near the Central American Seaway, linked to enhanced moisture transport. Compared to present-day, the zonal mean precipitation (Fig. 4) in the tropics increased by up to 913 mm/yr (2.5 mm/day) for the 6xCO₂ experiment and by 1204mm/yr (3.3 mm/day) for the 12xCO₂ experiment. Intensification of the downward branch of the Hadley cell and rise in temperature due to the increase in CO₂ radiative forcing relative to the 3xCO₂ simulation enhance latent and sensible heat fluxes, thus leading to higher aridity and more severe drought conditions (Fig. 9). Wind stress and barotropic stream function are decreased relative to the 3x CO₂ scenario, linked to polar amplification, and a reduced meridional temperature gradient in response to an increase in sea-ice albedo, land snow cover, and associated climate feedbacks. Trade winds (Fig. 5) and equatorial Ekman-induced upwelling declined by ~10-20% in the 6 x CO₂ scenario and by 30-50% in the 12x CO₂ scenario (Fig. 8), thus supporting an increase in equatorial surface temperature (Fig. 2 b) and a decline in the net primary and export production with an increase in radiative forcing (Winguth et., 2013). Compared to the 3xCO₂ latest Paleocene scenario, the mixed layer depth in the 6xCO₂ and 12xCO₂scenarios is further reduced (Fig. 6), leading to increased stratification and a collapse of the southern component deep water formation and meridional overturning circulation for the 12xCO₂ scenario (Fig. 8), with a shift form the thermal polar mode of deep-water formation to a subtropical haline shallow mode.

In contrast to the 3xCO₂ latest Paleocene scenario, the Arctic Ocean and water masses near Antarctica are ice-free in the 6xCO₂ PETM scenario, linked to elevated sea surface temperatures and the associated ice-albedo feedback as well as changes in ocean circulation.



3.4 The Sensitivity of Early Eocene Climate to Greenhouse Gas Forcing

The CESM1.2 equilibrium climate system sensitivity (ECS), defined as the ratio of the equilibrium temperature change to the doubling of the atmospheric CO₂, is 2.8 °C under Eocene boundary conditions (Fig. 10a), as compared to 3.2 °C for present-day conditions (Bitz et al., 2011). A climate sensitivity of 2.8 °C is comparable to the ECS in previous climate simulations using the climate community system model CCSM3 (Winguth et al., 2010; Lunt et al., 2012; Carmichael et al., 2016; Lunt et al. 2021), which range from 2.1°C to 4.1°C in the scenario with low cloud albedo feedback. Predicted global mean surface temperature for the 1xCO₂ scenario under Paleocene/Eocene boundary conditions exceeds the value inferred from the preindustrial scenario with CESM1.2 due to changes in geography, ice sheet-induced climate, and soil albedo forces. Differences between this study and early Eocene CCSM3 simulations (Winguth et al., 2010; Huber and Caballero, 2011; Kiehl and Shields, 2013) can be attributed to higher climate sensitivity of CESM1.2, an improved radiative transfer model, and differences in the soil albedo and aerosol forcing. Note that the CCSM3 prescribed present-day aerosol forcing including the anthropogenic perturbation, whereas this version of CESM1.2 applied the aerosol forcing of Herold et al. (2014), as estimated for the early Eocene. Discrepancies between this version CESM1.2 with Community Atmosphere Model Version 4 (CAM4) and CAM5 (Zhu et al., 2019; see also Fig. 1 in Lunt et al., 2021) are attributed to differences in cloud parameterizations and radiative transfer (Kay et al., 2012), surface albedo, and prescribed aerosol emissions resulting in higher climate sensitivity in CESM1.2 with CAM5.

4 Proxy- Model Comparisons

4.1 Surface Temperature

A suitable range of proxy data exists both for surface temperatures and precipitation. Data sets for temperature have been compiled as part of the DeepMIP by, e.g., Hollis et al. (2019) and references therein, for three selected time intervals: the LP, PETM, and early Eocene climatic optimum (EECO). Sea surface temperatures for Paleocene and Eocene have been compiled from oxygen isotopes, Mg/Ca values, clumped oxygen isotope values in well-preserved foraminifera in clay-rich sediments, and from Tex 86 in bulk sediment (Pearson et al., 2001; Sexton et al., 2006, Auderset et al., 2022). More details on the data and uncertainty as used in this study is given by Hollis et al. (2018) and literature cited therein.

The surface temperature is compared for two simulations, the 3x CO₂ scenario equivalent to latest Paleocene (LP) conditions, and the 6x CO₂ scenario representing the PETM, as suggested by DeepMIP protocol (Lunt et al., 2017). Comparison of simulated sea surface temperatures from the 3x CO₂ LP scenario with reconstructed paleo proxies on the location of the data (Fig. 11a) from the latest Paleocene reveals a strong positive correlation ($r = 0.748$, $p = 0.66$) for mean model values about 2.1 °C cooler at the proxy locations, primarily due to the high latitude bias. This p value is statically not significant because of the small sample size. The correlation of sea surface temperature between the 6x CO₂ PETM scenario (Fig. 11b) and corresponding PETM data of Hollis et al. (2019) ($r = 0.754$, $p = 0.35$) is also scattered, despite higher data size. Model-data biases of up to 8°C



and more occur at high latitudes, in particular at the data locations in the Arctic Ocean and New Zealand, potentially linked to
225 seasonal and/or diagenetic biases (Hollis et al., 2018, Lunt et al. 2021).

4.2 Precipitation

Mean annual precipitation (MAP) estimates from sedimentary proxy reconstructions and model simulations at the proxy sites
for the 3xCO₂ PAL LP and 6xCO₂ PAL PETM scenarios are shown in Figure 12. Proxy sedimentary reconstructions for the It
Paleocene, PETM, and early Eocene have been described in Carmichael et al. (2016) (their Table 3S). These proxies have been
230 compiled from oxygen isotopes from mammalian, fish, and foraminiferal fossils (Zachos et al., 2006; Zacke et al., 2009;
Clementz and Sewall, 2011), geomorphological data (John et al., 2008; Schmitz and Pujalte, 2007), biomarkers (Handley et
al., 2011; Pagani et al., 2006), other microfossils (Sluijs et al., 2011; Kender et al., 2012) and sedimentary-inferred precipitation
estimates (for example, Huber and Goldner, 2012). Simulated values within the 3x3 grid cells in the proximity of the proxy
locations have been averaged over these locations. The standard error has been compiled from the deviation of the mean from
235 these considered grid cells. Thus, a stronger gradient among the grid cell leads to a larger standard deviation and therefore a
larger error. The proxy-inferred estimates of precipitation are represented by a horizontal scale much smaller than resolved by
the inferred predictions from the simulations in this study.

In general, simulated values of MAP agree within the uncertainties of the paleo-precipitation estimates, particularly for the
Chicaloon Formation (Fig. 12b), Western Interior of the U.S. (Fig. 12e), Guchengzi Formations (Fig. 12f), Central Europe
240 (Fig. 12g), Laguna del Hunco (Fig. 12j) and Waipara River (Fig. 12k). Tropical precipitation appears to be sensitive to sea
surface temperature (and CO₂ radiative forcing), as identified for the Cerrejon Formation, Columbia (Fig. 12h), and also
suggested by analysis of present-day observations (e.g., Good et al. 2021, and references therein).

The model-data bias appears to be largest in the intertropical convergence zone (ITCZ, Fig. 12h) as well as at southern polar
latitudes (Fig. 12g), with a too low simulated precipitation compared to the observations, whereas CESM1.2 simulations
245 overestimated precipitation (as in previous studies, e.g., summarized by Carmichael et al., 2016). Note that data records span
wide time intervals from the late Paleocene to the Eocene Climate Optimum. Notably, paleo-precipitation estimates from
sedimentary records for the Antarctic Peninsula (see Figure 12 g) appear to be highly variable (with a range of ~70 cm/yr to
~260 cm/yr; Carmichael et al., 2016; their Table 3S). Uncertainties exist also about seasonal biases for paleo-precipitation.
Present-day simulated strong and very strong precipitation events in CESM1.2 are well reproduced, but model-data biases may
250 be associated with the simulated double ITCZ as indicated by Gent et al. (2011). This error also appears in the Eocene climate
simulations.

4.3 Deep Sea Ocean Circulation

In the following, simulated abyssal ocean circulation results will be evaluated with deep water mass tracers from the
sedimentary record. The distribution of stable carbon isotope ratios ($\delta^{13}\text{C}$) of dissolved inorganic carbon (DIC) in the ocean is
255 dominated by two effects, the fractionation by the air-sea gas exchange due to the tendency of the lighter isotope ¹²C to more



easily evaporate in dependence on the temperature (Mook et al., 1974; Broecker and Maier-Reimer et al., 1992), and the biological pump with $\delta^{13}\text{C}$ of DIC being correlated to phosphate below 1000 m (Kroopnick, 1985; Östlund et al., 1987, Winguth et al., 1999). However, this correlation may have been affected by a different fractionation of particulate organic matter in the past (Rau et al., 1991). An increased absence of water masses from the surface typically leads to an enrichment of ^{12}C and nutrients due to remineralization of particulate matter, thus deep present Pacific water masses are characterized by high phosphate and low $\delta^{13}\text{C}$ values. Analysis of stratigraphic reconstruction of $\delta^{13}\text{C}$ in planktonic and benthic foraminifera during the Early Eocene (Sexton et al. 2006) suggests that a lower-than-present vertical $\delta^{13}\text{C}$ gradient resulted from enhanced vertical mixing and thus a lower age in water masses in the abyss. Deep sea flow patterns inferred from $\delta^{13}\text{C}$ gradients indicate strong water mass formation around Antarctica including the South Atlantic (present Weddell Sea) and South Pacific (near the Eocene Australia) prior to the PETM and their decline during the PETM. Northern component water mass formations remained in the North Atlantic Ocean during the PETM (Nunes and Norris, 2006; Kirtland Turner et al., 2024) thus leading to a reversal of the deep-sea circulation in the Atlantic Ocean. Modelling results with CESM1.2 in this study support deep water formation in the South Atlantic (in the proximity of the present Weddell Sea) under Latest Paleocene conditions (3x CO_2 LP experiment) and a diminished Southern Ocean component water mass during the PETM (6x CO_2 PETM experiment). The decline of southern component water mass formation for the 6x CO_2 PETM experiment (Figure 13) is in agreement with the meridional trends inferred from the distribution of CaCO_3 dissolution horizons (Penman and Zachos, 2018; Zeebe and Zachos, 2007) and chert sedimentary records (Penman et al., 2018). It is noteworthy that the South Pacific deep-water formation is only simulated in the 1x CO_2 PD experiment (Figure 13a).

Neodymium isotope ratios ($^{143}\text{Nd}/^{144}\text{Nd}$ expressed as ϵ_{Nd} ; DePaolo and Wasserburg, 1976) from fish teeth have been commonly applied as a deep water mass tracer (Tachikawa et al., 1999; Martin and Scher, 2004; Thomas et al., 2003; Thomas 2004; Via and Thomas; 2006). Nd isotope data from sedimentary records of the Pacific Ocean are supportive of convective overturning in both polar hemispheres for the early Cenozoic (Thomas et al., 2014, McKinley et al., 2019). This study supports a separation of the sources of deep water in the South Pacific Ocean from those in the Atlantic Ocean but does not support polar deep-water source formation in the North Pacific Ocean (Figure 13 a-c). However, an inflow from the Central American Sea from the deep Atlantic to the Pacific Ocean could have ventilated the abyssal Pacific Ocean. Deep water formation in the North Pacific Ocean remains uncertain based on this study as well as on previous DeepMIP studies (Zhang et al., 2021). Data coverage of Nd isotopes for the Atlantic Ocean is limited and their analysis may favor bipolar deep-water formation. However, other studies suggest that deep water formation in the North Atlantic Ocean did not occur prior the middle Eocene (e.g., Boyle et al., 2017; Coxall et al., 2018; Gleason et al., 2009; Hohbein et al., 2012).

285 5 Summary and Conclusions

Climate sensitivity in this CESM1.2 simulation with CAM4 is comparable to previous CCSM3 simulations, but this study highlights several improvements in representing the climate change across the Paleocene-Eocene boundary and more



reasonably represents the observations. This is particularly the case for the prediction of temperatures in both the north and the south polar regions, and the substantially reduced pole-to-equator temperature gradient. The CESM1.2 also produces a better representation of tropical precipitation but underrepresents the proxy-inferred magnitude. This may be partially linked to the model resolution, but also to simulated warmer climate enhancing the water vapor saturation value in the atmosphere.

A shift from a southern-dominated deep-sea ventilation (thermal mode) at low atmospheric CO_2 radiative forcing of $1\text{-}3\times\text{CO}_2$ PAL to a less vigorous intermediate-to-shallow ventilation (haline mode) at atmospheric $p\text{CO}_2$ equal to or exceeding $6\times\text{CO}_2$ PAL has been simulated. A simulated decline in the southern component relative to the northern component water mass formation in response to CO_2 -radiative forcing during the onset of the PETM is consistent with carbon isotopes, CaCO_3 dissolution horizons, and change in the chert sedimentary record. However, a bipolar deep-sea ventilation as suggested from Nd isotope ratios cannot be supported by this as well as other DeepMIP studies (Zhang et al. 2021). The lack of Antarctic ice during the late Paleocene/early Eocene and associated reduced pole-to-equator temperature gradient affects the strength of wind stress and thus the strength of the barotropic stream function, enhancing the stratification close to Antarctica.

Reduced Ekman-induced wind stress over the tropics contributes to reduced upwelling and thus favors a reduced paleo productivity in that region. Decline in deep-sea ventilation and oxygen solubility due to ocean warming would have caused a decline of dissolved oxygen concentrations in the abyssal ocean (Nicolo et al., 2010; Schmidko et al., 2017; Ito et al., 2017; Winguth et al., 2013) and enhanced benthic extinctions during the onset of the PETM. However, dissolved oxygen concentration in the upper tropical ocean may have increased during the PETM at least regionally due to decreased upwelling and productivity (Moretti et al., 2014). This greater response in ocean stratification due to an increase in CO_2 radiative forcing is linked to higher climate sensitivity and improved cloud feedbacks of CESM1.2 compared to CCSM3.

Data Availability

Data will be provided by the corresponding author upon request.

Author contributions

AW performed climate simulations and analysis, and CS provided boundary conditions including aerosol forcing and land surface maps for the simulations. MB did postprocessing and averaging of climate simulation and analysis for the $1\times\text{CO}_2$ PB scenario. PH, ET, AW, and CW discussed the results. AW wrote the paper, and all authors provided input for the paper before submission.



Competing Interest

315 Arne M.E. Winguth is a member of the editorial board of the journal “Climate of the Past”. The other authors declare that they have no conflict of interest.

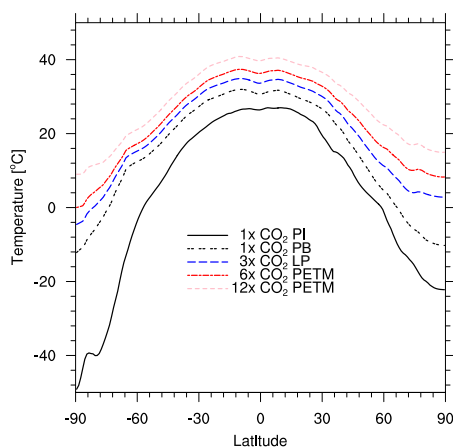
Acknowledgements. This research used samples and data provided by the International Ocean Discovery Program (IODP). Funding for this research was provided by National Science Foundation (NSF) grants OCE-1536630 to A. Winguth and E. Griffith and OCE-1536611 to E. Thomas and by Heising-Simons Foundation Grant #2016-004. We acknowledge high-
320 performance computing support from the Cheyenne: HPE/SGI ICE XA System (doi:10.5065/D6RX99HX) and from the Casper system (<https://ncar.pub/casper>) provided by the NSF National Center for Atmospheric Research (NCAR), sponsored by the National Science Foundation.



Table 1. List of experiments for the climate simulations

Experiment	pCO ₂	Aerosol	SAT	TS Land	TOA ²⁾
	[ppmv]	forcing	[°C]	[°C]	[W m ⁻²]
Preindustrial (PI)	280	1850	14.8	8.0	-0.555
1xCO ₂ Paleocene	280	PETM ¹⁾	22.2	16.7	-0.554
Baseline (PB)					
3xCO ₂ Latest	840	PETM	26.0	22.1	-0.290
Paleocene (LP)					
6xCO ₂ PETM	1680	PETM	28.9	26.4	0.023
12xCO ₂ PETM	3360	PETM	33.0	32.5	0.270

325 ¹⁾ see Herold et al. (2014); ²⁾ top of atmosphere energy balance



330 **Figure 1.** Zonal average mean annual surface air temperature simulated by CESM1.2 for the preindustrial experiment (PI; black), Paleocene Baseline (PB) simulation at 1xCO₂ PAL (double dashed black), latest Paleocene (LP) at 3xCO₂ PAL (dashed blue), PETM 6xCO₂ PAL (red, dash-dotted), and PETM 12xCO₂ PAL (light red, dash) experiment.

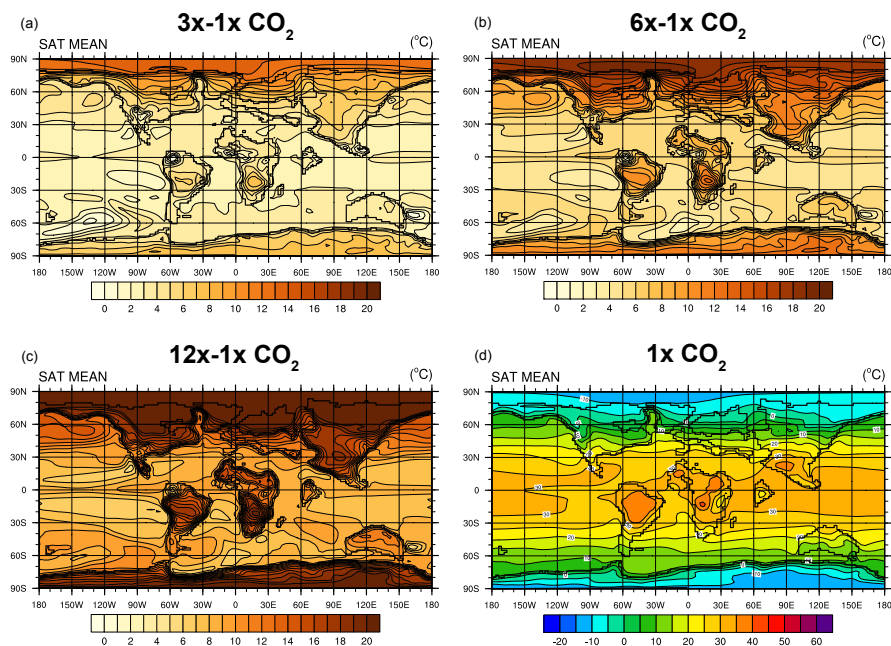


Figure 2. Difference in mean annual 2m surface air temperature in °C simulated by CESM1.2 between (a) LP at 3xCO₂ PAL, (b) PETM at 6 xCO₂ PAL, and (c) PETM at 12 xCO₂ PAL and PB at 1xCO₂ PAL experiment. (d) PB at 1xCO₂ PAL

335 scenario is shown for reference.

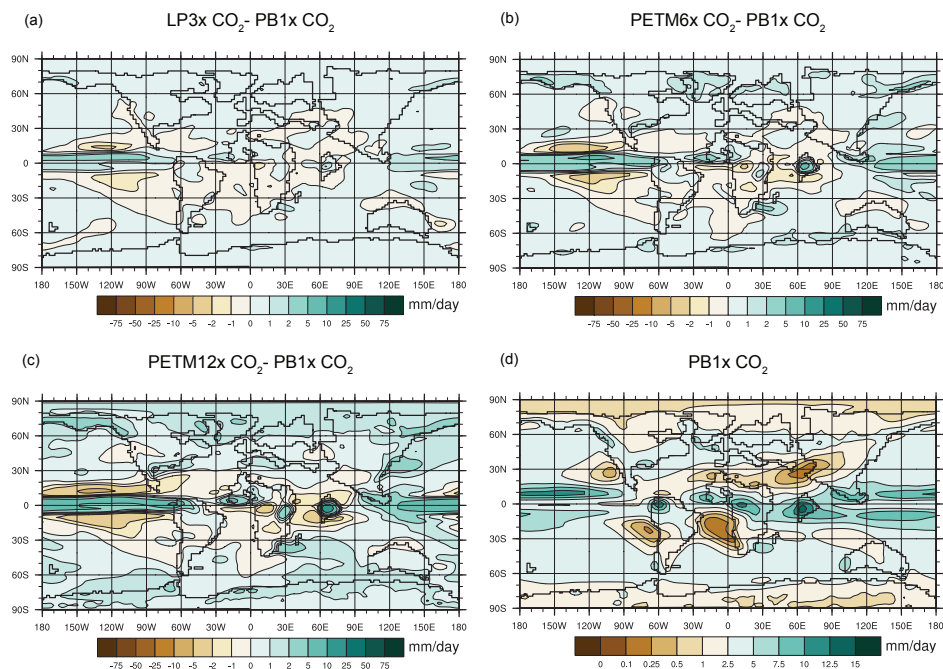


Figure 3. Difference in mean annual precipitation in mm day⁻¹ simulated by CESM1.2 between (a) LP at 3xCO₂ PAL, (b) PETM at 6 xCO₂ PAL, and (c) PETM at 12 xCO₂ PAL and PB at 1xCO₂ PAL experiment. PB at 1xCO₂ PAL scenario is shown for reference.

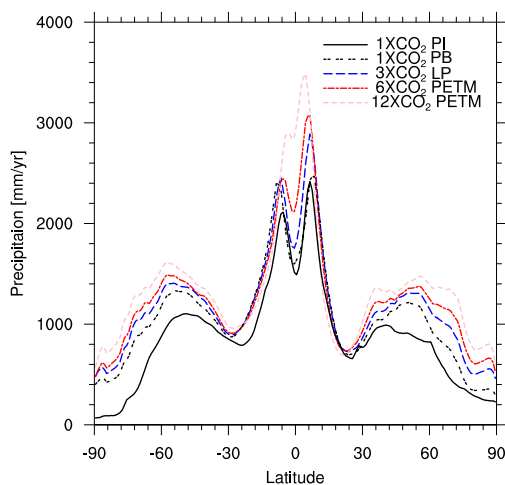


Figure 4. Zonal average 2 m surface mean annual precipitation simulated by CESM1.2 for the preindustrial experiment (PI; black), Paleocene Baseline (PB) simulation at 1xCO₂ PAL (double dashed black), Latest Paleocene (LP) at 3xCO₂ PAL (dashed blue), PETM 6xCO₂ PAL (red, dash-dotted), and PETM 12xCO₂ PAL (light red, dash) experiment.

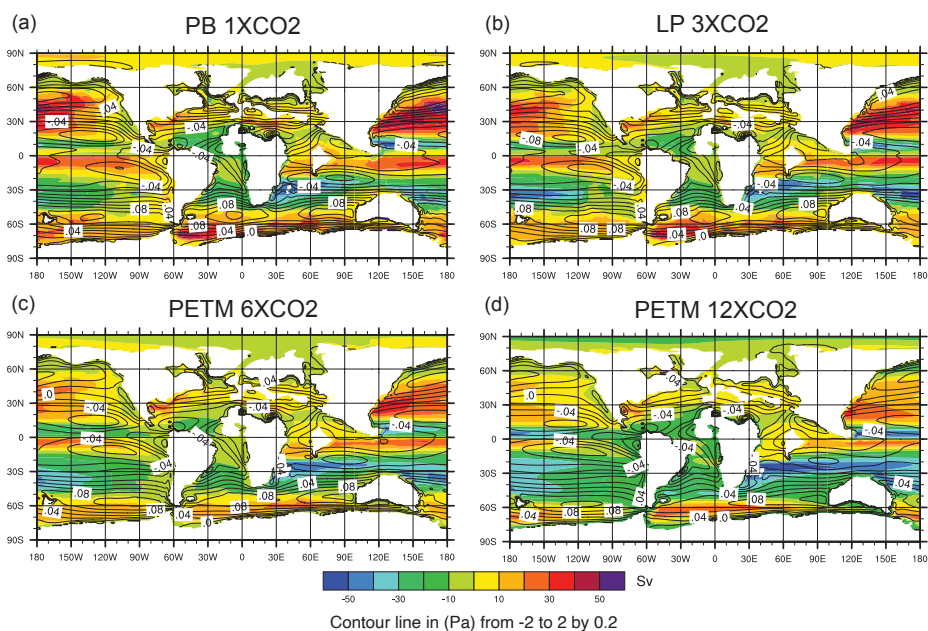




Figure 5. Mean annual barotropic stream function in Sv ($1 \text{ Sv} = 10^6 \text{ m}^3 \text{ s}^{-1}$; contour shades) and zonal wind stress in Pa (contour lines) simulated by CESM1.2 between (a) PB at $1x\text{CO}_2$ PAL, (b) LP at $3x\text{CO}_2$ PAL, (c) PETM at $6x\text{CO}_2$ PAL, and (d) PETM at $12x\text{CO}_2$ PAL experiment.

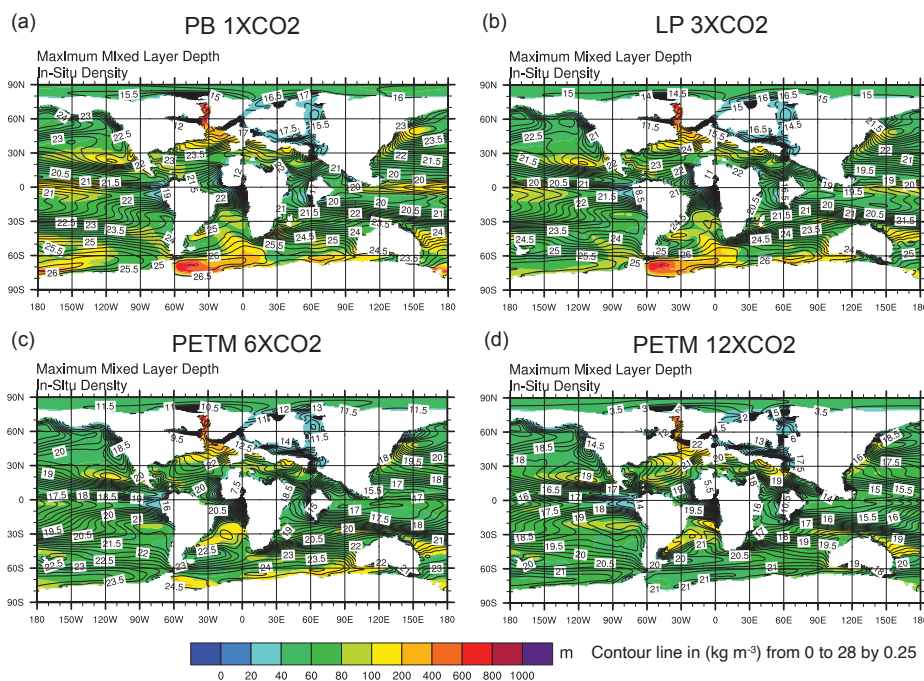
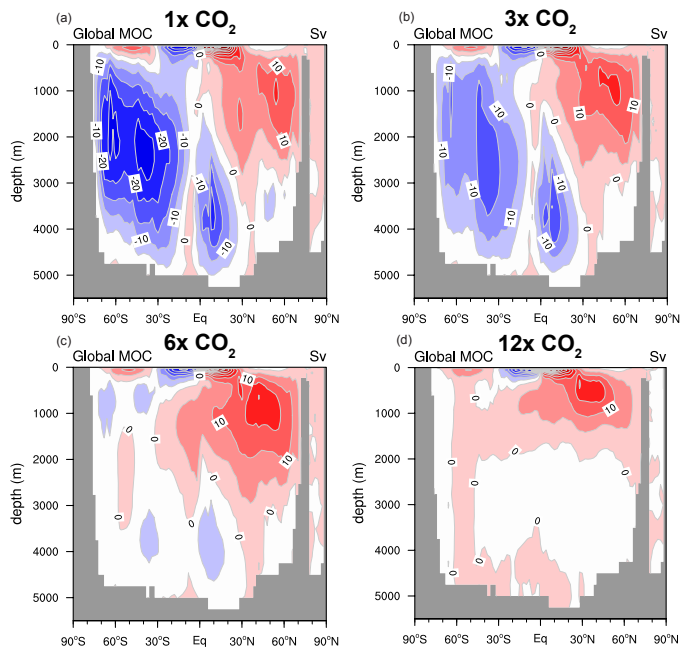
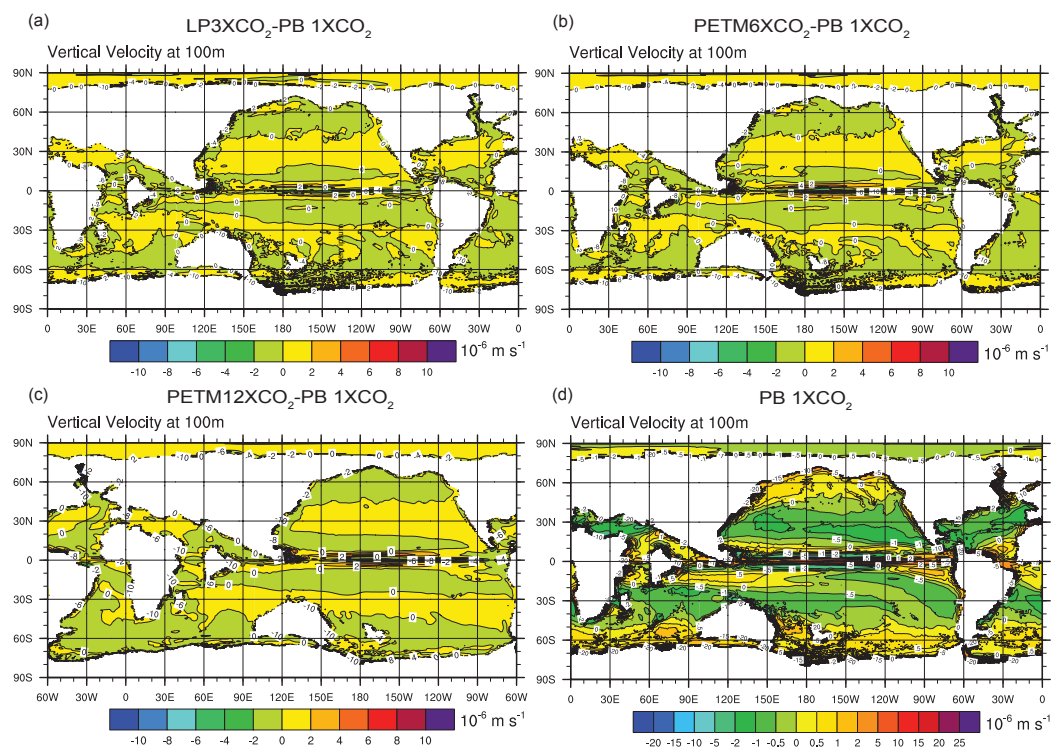


Figure 6. Mean maximum mixed layer depth in m (contour shades) and In-Situ Density σ_t in kg m^{-3} (contour lines) simulated by CESM1.2 between (a) PB at $1x\text{CO}_2$ PAL, (b) LP at $3x\text{CO}_2$ PAL, (c) PETM at $6x\text{CO}_2$ PAL, and (d) PETM at $12x\text{CO}_2$ PAL experiment.

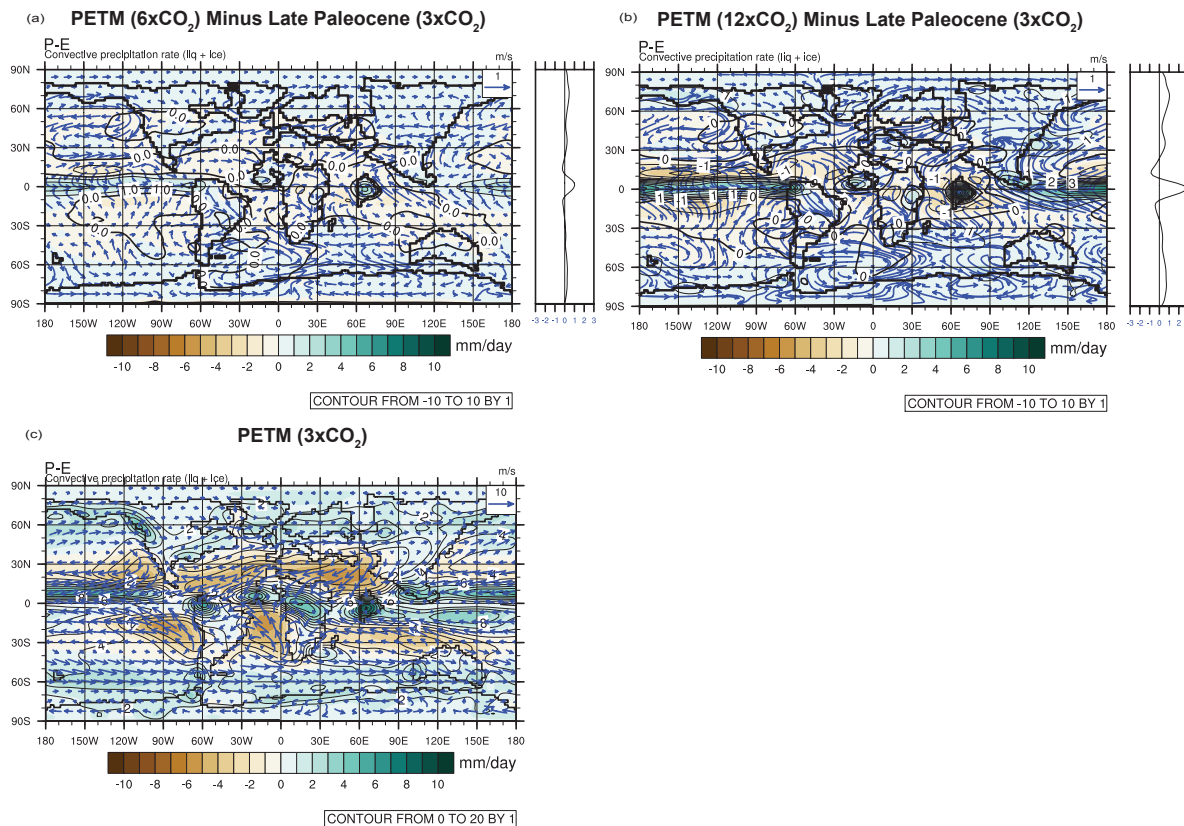


360

Figure 7. Mean annual global meridional barotropic stream function in Sv simulated by CESM1.2 between (a) PB at 1xCO₂ PAL, (b) LP at 3xCO₂ PAL, (c) PETM at 6 xCO₂ PAL, and (d) PETM at 12 xCO₂ PAL experiment.



365 **Figure 8.** Mean annual global upwelling in 100 m in 10^{-6} m s^{-1} simulated by CESM1.2. Difference between (a) LP at $3x\text{CO}_2$ PAL and PB at $1x\text{CO}_2$ PAL scenarios, (b) PETM at $6x\text{CO}_2$ PAL and PB at $1x\text{CO}_2$ PAL scenarios, (c) PETM at $12x\text{CO}_2$ PAL and PB at $1x\text{CO}_2$ PAL scenarios, (d) PB at $1x\text{CO}_2$ PAL.



370

Figure 9. Difference in mean annual precipitation minus evaporation (contour shades) in mm day^{-1} , precipitation (contour lines) in mm day^{-1} , and wind speed (vectors) simulated by CESM1.2 between (a) PETM at 6 xCO₂ PAL and LP at 3xCO₂ PAL experiment, (b) PETM at 6 xCO₂ PAL and LP at 3xCO₂ PAL experiment, and (c) LP at 3 xCO₂ PAL scenario. Wind speed vector length for (a) and (b) is 1 m s^{-1} and for (c) 10 m s^{-1} .

375

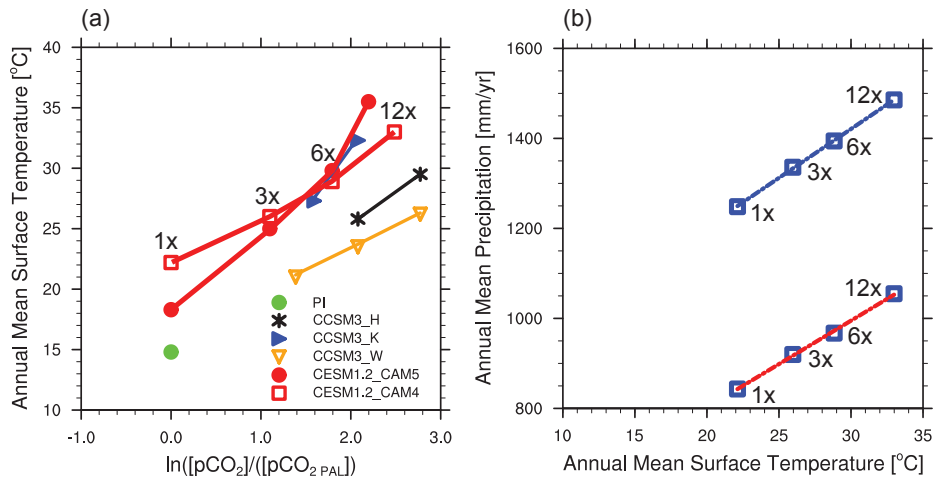


Figure 10. (a) Mean annual surface temperature as a function of the natural logarithm of the atmospheric pCO_2 relative to the pCO_2 at preindustrial levels. For comparison, simulations of CCSM3_W (Winguth et al., 2010), CCSM_H (Huber and Caballero, 2011), CCSM3_K (Kiehl and Shields, 2013), and CESM1.2 with CAM5 (Zhu et al., 2019) are shown. (b) Annual mean precipitation (blue) and convective precipitation (red) for CESM1.2 (this study) in relation to annual mean 2m surface air temperature.

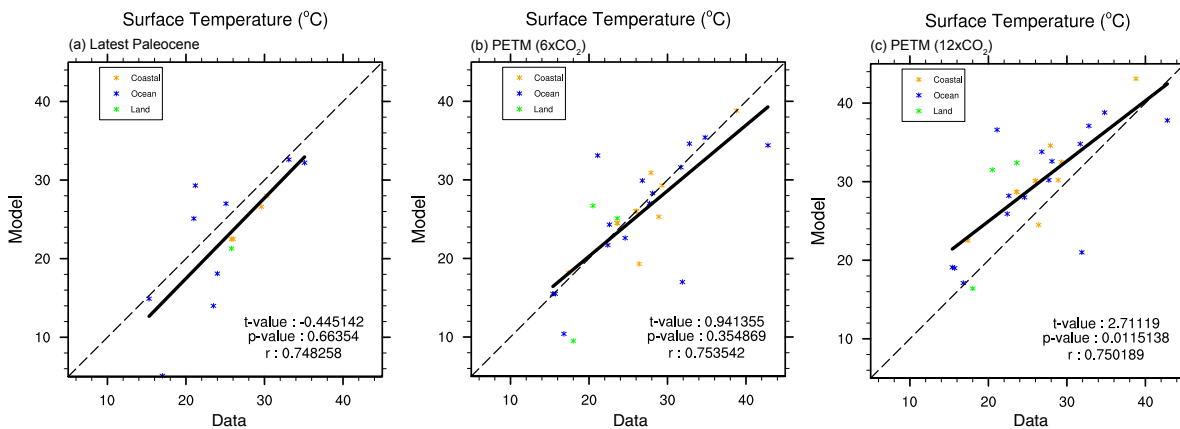
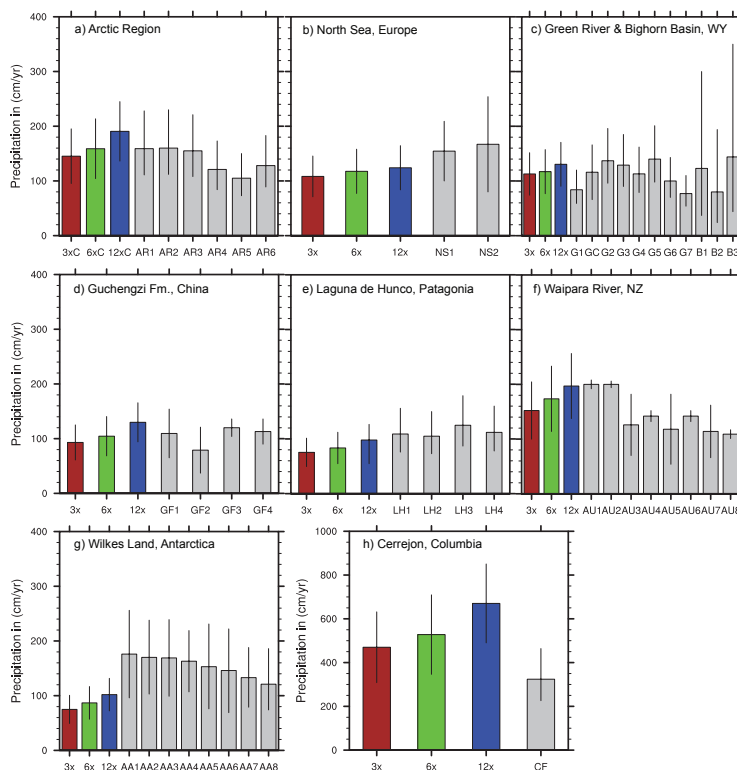


Figure 11. Pearson correlation between compiled temperature reconstructions (data from Hollis et al., 2019; orange star coastal, blue star ocean, and green star land sites) (a) for the Latest Paleocene and the CESM1.2 LP at 3xCO₂ PAL scenario, (b) for the PETM and the CESM1.2 PETM at 6xCO₂ scenario, and (c) for the PETM and the CESM1.2 PETM at 12xCO₂ scenario.



390 **Figure 12.** Comparison of mean annual precipitation between Late Paleocene/Early Eocene proxy data (grey) and CESM1.2
 LP 3x CO₂ (red), PETM 6x CO₂ (green), and PETM 12x CO₂ (green) experiments at the proxy sites for (a) Arctic region
 including Chicaloon Formation, Alaska (AR1-AR4), Arkrose Ridge Formation, Alaska (AR5, Sunderlin et al. 2011), and
 Northwest Territory (AR6, Greenwood et al. 2010); (b) North Sea, Europe (NS1-NS2; Eldrett et al., 2014), (c) Green River
 Basin (G1-G7; Wilf et al., 1998; and Wilf, 2000; and GC; Wing and Greenwood, 1993) and Big Horn Basin (B1-B3, Wing
 395 et al. 2005) in Wyoming, North America, (d) Guchengzi Formation, Fushun, China,(GF1-GF4; Wang 2010; Wang et al.
 2013; and Quan et al., 2011), (e) Laguna de Hunco, S. America (LH1-LH4; Wilf et al., 2005), (f) Waipara River in New
 Zealand (NZ1-NZ8; Pancost et al. 2013), and (g) Wilkes Land Sector, Antarctic Peninsula (AA1-AA7; Pross et al. 2012).
 Note that the scale needed to be adjusted for (h). For the geographic position of the proxy records and details see text and
 Table S3 in Carmichael et al. (2016).

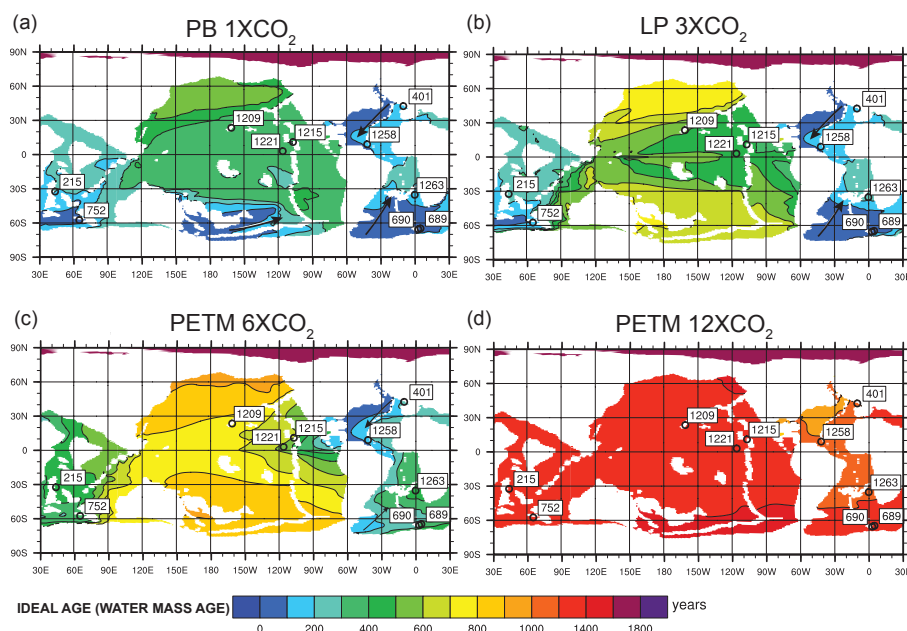


Figure 13. Ideal age water mass tracer in years simulated by CESM1.2 between (a) PB at 1xCO₂ PAL, (b) LP at 3xCO₂ PAL, (c) PETM at 6 xCO₂ PAL, and (d) PETM at 12 xCO₂ PAL experiment. Arrows denotes flow direction of deep water and circles with numbers refer to location of sedimentary records from IODP deep water mass proxies (see references in section 4.1).

References

- Abbot, D.S., Huber, M., Bousquet, G., and Walker, C.C.: High-CO₂ cloud radiative forcing feedback over both land and ocean in a global climate model, *Geophys. Res. Lett.*, 36, L05702, doi:10.1029/2008GL036703, 2009.
- 410 Boyle, P.R., Romans, B. W., Tucholke, B.E., Norris, R.D., Swift, S.A., and Sexton, P.F.: Cenozoic North Atlantic deep circulation history recorded in contourite drifts, offshore Newfoundland, Canada, *Marine Geology*, 385, 185–203. <https://doi.org/10.1016/j.margeo.2016.12.014>, 2017.
- Barron, E.J., Washington, W.M.: Atmospheric circulation during warm geologic periods: is the equator-to-pole surface-temperature gradient the controlling factor? *Geology* 10, 633–636, 1982.
- 415 Brown, M.: Climate Change of the South Polar Region in Response to Topographic and Cryospheric Forcings During the Paleocene-Eocene Thermal Maximum, M.S. Thesis, University of Texas Arlington, 46 p., Available online: <http://hdl.handle.net/10106/28096>, 2019.
- Bowen, G., Maibauer, B., Kraus, M. et al.: Two massive, rapid releases of carbon during the onset of the Palaeocene–Eocene thermal maximum, *Nature Geosci.*, 8, 44–47, <https://doi.org/10.1038/ngeo2316>, 2015.
- 420 Broecker, W.S., and Maier-Reimer, E.: The influence of air and sea exchange on the carbon isotope distribution in the sea, *Global Biochem. Cy.*, 6(3), 315–320, <https://doi.org/10.1029/92GB01672>, 1992.
- Carmichael, M. J., Lunt, D. J., Huber, M., Heinemann, M., Kiehl, J. T., LeGrande, A., Heinemann, M., Kiehl, J., LeGrande, A., Loptson, C.A., Roberts, C.D., Sagoo, N., Shields, C., Valdes, P.J., Winguth, A., Winguth, C., and Pancost, R. D.: A



- 425 model-model and data-model comparison for the early Eocene hydrological cycle, *Climate of the Past*, 12, 455–481.
doi:10.5194/cp-12-455-2016, 2016.
- Clementz, M.T. and Sewall, J.O.: Latitudinal gradients in greenhouse seawater $\delta^{18}\text{O}$: evidence from Eocene sirenian tooth enamel, *Science* 332(6028):455–8. doi: 10.1126/science.1201182, 2011.
- Coxall, H. K., Huck, C. E., Huber, M., Lear, C. H., Legarda-Lisarri, A., & O'Regan, M.: Export of nutrient rich northern component water preceded early Oligocene Antarctic glaciation, *Nature Geoscience*, 11(3), 190–196.
430 <https://doi.org/10.1038/s41561-018-0069-9>, 2018.
- DeConto, R. M., Galeotti, S., Pagani, M., Tracy, D., Schaefer, K., Zhang, T., Polgaard, D., and Beerling, D. J.: Past extreme warming events linked to massive carbon release from thawing permafrost, *Nature* 484: 87–91, doi: 10.1038/nature10929, 2012.
- DePaolo, D. J. and Wasserburg, G. J.: Nd isotopic variations and petrogenetic models. *Geophys. Res. Lett.* 3, 248–252, 1976.
- 435 Dickens, G.R.: Down the Rabbit Hole: toward appropriate discussion of methane release from gas hydrate systems during the Paleocene-Eocene thermal maximum and other past hyperthermal events, *Climate of the Past*, 7, 831–846, 2011.
- Dunkley Jones, T., D. J. Lunt, D. N. Schmidt, A. Ridgwell, A. Sluijs, P. J. Valdez, and M. A. Maslin: Climate model and proxy data constraints on ocean warming across the Paleocene–Eocene Thermal Maximum, *Earth-Science Reviews*, 125, 123–145, 2013.
- 440 Eldrett, J. S., Greenwood, D. R., Polling, M., Brinkhuis, H., and Sluijs, A.: A seasonality trigger for carbon injection at the Paleocene-Eocene Thermal Maximum, *Clim. Past*, 10, 759–769, doi:10.5194/cp-10-759-2014, 2014.
- Elsworth, G., Galbraith, E., Halverson, G., and Yang, S.: Enhanced weathering and CO_2 drawdown caused by latest Eocene strengthening of the Atlantic meridional overturning circulation, *Nature Geoscience*, 10(3), 213–216.
<https://doi.org/10.1038/ngeo2888>, 2017.
- 445 Gent, P. R., G. Danabasoglu, L. J. Donner, M. M. Holland, E. C. Hunke, S. R. Jayne, D. M. Lawrence, R. B. Neale, P. J. Rasch, M. Vertenstein, P. H. Worley, Z.-L. Yang, and M. Zhang: The Community Climate System Model version 4, *Journal of Climate* 24, 4973–4991, 2011.
- Gleason, J.D., Thomas, D.J., Moore, T.C., Blum, J.D., Owen, R.M., and Haley, B.A.: Early to middle Eocene history of the Arctic Ocean from Nd-Sr isotopes in fossil fish debris, Lomonosov Ridge. *Paleoceanography*, 24(2).
450 <https://doi.org/10.1029/2008PA001685>, 2009.
- Goldner, A., Herold, N., and Huber, M.: Antarctic glaciation caused ocean circulation changes at the Eocene-Oligocene transition, *Nature*, 511:7511, 574–577, <https://doi.org/10.1038/nature13597>, 2014.
- Good, P., Chadwick, R., Holloway, C.E., Kennedy, J., Lowe, J.A., Roehrig R. and Stephanie, S., Rushley, S.S.: High sensitivity of tropical precipitation to local sea surface temperature, *Nature* 589(7842): 408–414, <https://doi.org/10.1038/s41586-020-2887-3>, 2021.
- 455 Greenwood, D. R., Basinger, J. F., and Smith, R. Y.: How wet was the Arctic Eocene rain forest? Estimates of precipitation from Paleogene Arctic macrofloras, *Geology*, 38, 15–18, doi:10.1130/G30218.1, 2010.
- Gutjahr, M., Ridgwell, A., Sexton, P., Anagnostou, E., Pearson, P.N., Pälike, H., Norris, R.D., Thomas, E., and Foster, G.L.: Very large release of mostly volcanic carbon during the Palaeocene–Eocene Thermal Maximum, *Nature* 548, 573–577,
460 [doi: 10.1038/nature23646](https://doi.org/10.1038/nature23646), 2017.
- Handley, L., Crouch, E. M., and Pancost, R. D.: A New Zealand record of sea level rise and environmental change during the Paleocene–Eocene Thermal Maximum, *Palaeogeogr. Palaeoclimatol.*, 305, 185–200, doi:10.1016/j.palaeo.2011.03.001, 2011.
- Held, I. M. and Soden, B. J.: Robust responses of the hydrological cycle to global warming, *J. Climate*, 19, 5686–5699, doi:10.1175/JCLI3990.1, 2006.
- 465 Herold N., Buzan, J. Seton, M. Goldner, A.Green, . J.A.M. Müller, R.D., Markwick P., and Huber, M.: A suite of Early Eocene (55 Ma) climate model boundary conditions, *Geosci. Model Dev. Discuss.*, 7, 529–562, 2014.
- Hohbein, M. W., Sexton, P. F., & Cartwright, J. A.: Onset of North Atlantic Deep Water production coincident with inception of the Cenozoic global cooling trend, *Geology*, 40(3), 255–258. <https://doi.org/10.1130/G32461>, 2012.
- Hollis, C. J., Dunkley Jones, T., Anagnostou, E., Bijl, P. K., Cramwinkel, M. J., Cui, Y., Dickens, G. R., Edgar, K. M., Eley, Y., Evans, D., Foster, G. L., Frieling, J., Inglis, G. N., Kennedy, E. M., Kozdon, R., Laurentano, V., Lear, C. H., Littler, K., Lourens, L., Meckler, A. N., Naafs, B. D. A., Pälike, H., Pancost, R. D., Pearson, P. N., Röhl, U., Royer, D. L., Salzmann, U., Schubert, B. A., Seebeck, H., Sluijs, A., Speijer, R.P., Stassen, P., Tierney, J., Tripathi, A., Wade, B., Westerhold, T., Witkowski, C., Zachos, J. C., Zhang, Y. G., Huber, M., and Lunt, D. J.: The DeepMIP contribution to PMIP4:



- 475 methodologies for selection, compilation and analysis of latest Paleocene and early Eocene climate proxy data, incorporating version 0.1 of the DeepMIP database, *Geosci. Model Dev.*, 12, 3149–3206, <https://doi.org/10.5194/gmd-12-3149-2019>, 2019.
- Huber, M.: Climate change. A hotter greenhouse?, *Science*, 321, 353–354, doi:10.1126/science.1161170, 2008.
- Huber, M. and Goldner, A.: Eocene monsoons, *J. Asian Earth Sci.*, 44, 3–23, doi:10.1016/j.jseaes.2011.09.014, 2012.
- Huber, M. and Caballero, R.: The early Eocene equable climate problem revisited, *Clim. Past*, 7, 603–633, <https://doi.org/10.5194/cp-7-603-2011>, 2011.
- 480 Hurrell, J. W., Holland, M. M., Gent, P. R., Ghan, S., Kay, J. E., Kushner, P. J., Lamarque, J. F., Large, W. G., Lawrence, D., Lindsay, K., Lipscomb, W. H., Long, M. C., Mahowald, N., Marsh, D. R., Neale, R. B., Rasch, P., Vavrus, S., Vertenstein, M., Bader, D., Collins, W. D., Hack, J. J., Kiehl, J. T., and Marshall, S.: The community earth system model: A framework for collaborative research, *B. Am. Meteorol. Soc.*, 94, 1339–1360, <https://doi.org/10.1175/BAMS-D-12-00121.1>, 2013.
- 485 Inglis, G. N., Farnsworth, A., Lunt, D., Foster, G. L., Hollis, C. J., Pagani, M., et al.: Descent toward the icehouse: Eocene Sea surface cooling inferred from GDGT distributions. *Paleoceanography*, 30, 1000–1020. <https://doi.org/10.1002/2014PA002723>, 2015.
- John, C. M., Bohaty, S. M., Zachos, J. C., Sluijs, A., Gibbs, S., Brinkhuis, H., and Bralower, T. J.: North American continental margin records of the Paleocene–Eocene thermal maximum: implications for global carbon and hydrological cycling, *Paleoceanography*, 23, Pa2217, doi:10.1029/2007pa001465, 2008.
- 490 Kay, J. E., Hillman, R., Klein, A., Zhang Y., Medeiros, B. Pincus, R., Gettelman A., Eaton B. Boyle J., Marchand R., and Ackerman T.P.: Exposing global cloud biases in the Community Atmosphere Model (CAM) using satellite observations and their corresponding instrument simulators, *Journal of Climate*, 25, 5190–5207, doi: 10.1175/JCLI-D-11-00469.1, 2012.
- Kennett, J.P., and L.D. Stott: Abrupt deep-sea warming, palaeoceanographic changes and benthic extinctions at the end of the Palaeocene, *Nature*, 353, 225–229, 1991.
- 495 Kender, S., Stephenson, M. H., Riding, J. B., Leng, M. J., Knox, R. W. O. B., Peck, V. L., Kendrick, C. P., Ellis, M. A., Vane, C. H., and Jamieson, R.: Marine and terrestrial environmental changes in NW Europe preceding carbon release at the Paleocene–Eocene transition, *Earth Planet. Sc. Lett.* 353–354, 108–120, doi:10.1016/j.epsl.2012.08.011, 2012.
- Kump, L.R., and Pollard, D.: Amplification of Cretaceous warmth by biological cloud feedbacks, *Science*, 320, 195, 2008.
- 500 Kiehl, J. T. and Shields, C. A.: Sensitivity of the Palaeocene–Eocene Thermal Maximum climate to cloud properties, *Philos. T. Roy. Soc. A*, 371, 20130093, doi:10.1098/rsta.2013.0093, 2013.
- Kirtland Turner, S., Ridgwell, A., Keller, A.L., Vahlenkamp, M., Aleksinska, A.K, Sexton, P.F., Penman, D.E., Hull, P.M., and Norris, R.D.: Sensitivity of ocean circulation to warming during the Early Eocene greenhouse, *Proc. Nat. Ac. Sci.*, 121(24), 1–8, <https://doi.org/10.1073/pnas.2311980121>, 2024
- 505 Kroopnick, P. M.: The distribution of ^{13}C of ΣCO_2 in the world oceans, *Deep Sea Research Part A. Oceanographic Research Papers*, 32(1), 57–84. [https://doi.org/10.1016/0198-0149\(85\)90017-2](https://doi.org/10.1016/0198-0149(85)90017-2), 1985.
- Lefebvre, V., Donnadiou, Y., Sepulchre, P., Swingedouw, D., and Zhang, Z.-S.: Deciphering the role of southern gateways and carbon dioxide on the onset of the Antarctic Circumpolar Current, *Paleoceanography*, 27, PA4201. <https://doi.org/10.1029/2012PA002345>, 2012.
- 510 Lunt, D.J., Dunkley Jones, T., Heinemann, M., Huber, M., LeGrande, A., Winguth, A., Loptson, C., Marotzke, J., Tindall, J., Valdes, P., and Winguth, C.: A model-data comparison for a multi-model ensemble of early Eocene Atmosphere–Ocean simulations: EoMIP, *Climates of the Past* 8, 1717–1736, 2012.
- Lunt, D. J., Huber, M., Anagnostou, E., Baatsen, M. L. J., Caballero, R., DeConto, R., Dijkstra, H. A., Donnadiou, Y., Evans, D., Feng, R., Foster, G. L., Gasson, E., von der Heydt, A. S., Hollis, C. J., Inglis, G. N., Jones, S. M., Kiehl, J., Kirtland Turner, S., Korty, R. L., Kozdon, R., Krishnan, S., Ladant, J.-B., Langebroek, P., Lear, C. H., LeGrande, A. N., Littler, K., Markwick, P., Otto-Bliesner, B., Pearson, P., Poulsen, C. J., Salzmann, U., Shields, C., Snell, K., Stärz, M., Super, J., Tabor, C., Tierney, J. E., Tourte, G. J. L., Tripathi, A., Upchurch, G. R., Wade, B. S., Wing, S. L., Winguth, A. M. E., Wright, N. M., Zachos, J. C., and Zeebe, R. E.: The DeepMIP contribution to PMIP4: experimental design for model simulations of the EECO, PETM, and pre-PETM (version 1.0), *Geosci. Model Dev.*, 10, 889–901, <https://doi.org/10.5194/gmd-10-889-2017>, 2017.
- 520 Lunt, D. J., Bragg, F., Chan, W.-L., Hutchinson, D.K., Ladant, J.-B., Niezgodzki, I., et al.: DeepMIP: Model intercomparison of early Eocene climatic optimum (EECO) large-scale climate features and comparison with proxy data, *Clim. Past* 17, 203–227. doi:10.5194/cp-17-203-2021, 2021.



- 525 Inglis, G. N., Bragg, F., Burls, N. J., Cramwinckel, M. J., Evans, D., Foster, G. L., Huber, M., Lunt, D. J., Siler, N., Steinig,
S., Tierney, J. E., Wilkinson, R., Anagnostou, E., de Boer, A. M., Dunkley Jones, T., Edgar, K. M., Hollis, C. J.,
Hutchinson, D. K., and Pancost, R. D.: Global mean surface temperature and climate sensitivity of the early Eocene
Climatic Optimum (EECO), Paleocene–Eocene Thermal Maximum (PETM), and latest Paleocene, *Clim. Past*, 16, 1953–
1968, <https://doi.org/10.5194/cp-16-1953-2020>, 2020.
- 530 Ito, T., Minobe, S., Long, M.C., and Deutsch, C.: Upper ocean O₂ trends: 1958–2015, *Geophys. Res. Lett.*, 44, 4214–4223,
2017.
- Martin, E. E. and Scher, H. D.: Preservation of seawater Sr and Nd isotopes in fossil fish teeth: bad news and good news, *Earth
Planet. Sci. Lett.* 220, 25–39, 2004.
- Meehl, G.A., Washington, W.M., Arblaster, J.M., Hu, A. Teng, H., Kay, J.E., Gettleman, A., Lawrence, D.M., Sanderson,
B.M., Strand, W.G.: Climate Projections in CESM1(CAM5) compared to CCSM4, *J. Climate*, 26, 6287–6308,
535 <https://doi.org/10.1175/CLI-D-12-00572.1>, 2013.
- Mikolajewicz, U., Maier-Reimer, E., Crowley, T.J., and Kim, K.-Y.: Effect of drake and Panamanian gateways on the
circulation of an ocean model, *Paleoceanography*, 8(4), 409–426, <https://doi.org/10.1029/93PA00893>, 1993.
- Mook, W.G., Bommerson J.C., Staverman W.H.: Carbon isotope fractionation between dissolved bicarbonate and gaseous
carbon dioxide, *Earth Planet. Sc. Lett.*, 22(2), 196–176, [https://doi.org/10.1016/0012-821X\(74\)90078-8](https://doi.org/10.1016/0012-821X(74)90078-8), 1974.
- 540 Nicolo, M., Dickens, G.R., and Hollis, C.J.: South Pacific intermediate water oxygen depletion at the onset of the Paleocene–
Eocene thermal maximum as depicted in New Zealand margin sections, *Paleoceanography*, 25, PA4210,
doi:10.1029/2009PA001904, 2010.
- Nong, G. T., Najjar, R. G., Seidov, D., and Peterson, W. H.: Simulation of ocean temperature change due to the opening of
Drake Passage, *Geophysical Research Letters*, 27(17), 2689–2692, <https://doi.org/10.1029/1999GL011072>, 2000.
- 545 Nunes, F., and Norris, R. D.: Abrupt reversal in ocean overturning during the Palaeocene/Eocene warm period. *Nature*,
439(7072), 60–63, <https://doi.org/10.1038/nature04386>, 2006.
- Pagani, M., N. Pedentchouk, M. Huber, A. Sluijs, S. Schouten, H. Brinkhuis, J. S. Sinninghe Damsté, G. R. Dickens, and the
Expedition 302 Scientists: Arctic hydrology during global warming at the Paleocene/Eocene thermal maximum, *Nature*,
442, 671–675, 2006.
- 550 Pancost, R. D., Taylor, K. W. R., Inglis, G. N., Kennedy, E. M., Handley, L., Hollis, C. J., Crouch, E. M., Pross, J., Huber, M.,
Schouten, S., Pearson, P. N., Morgans, H. E. G., and Raine, J.I.: Early Paleogene evolution of terrestrial climate in the SW
Pacific, Southern New Zealand, *Geochem. Geophys. Geosyst.*, 14, 5413–5429, doi:10.1002/2013gc004935, 2013.
- Penman, D. E., Hoenisch, B., Zeebe, R.E., Thomas, E., Zachos, J.C.: Rapid and sustained surface ocean acidification during
the Paleocene-Eocene Thermal maximum, *Paleoceanography*, 29: 357–369, 2014.
- 555 Pross, J., Contreras, L., Bijl, P. K., Greenwood, D. R., Bohaty, S.M., Schouten, S., Bendle, J. A., Rohl, U., Tauxe, L., Raine,
J. I., Huck, C. E., van de Flierdt, T., Jamieson, S. S. R., Stickley, C. E., van de Schootbrugge, B., Escutia, C., Brinkhuis,
H., and IODP Expedition 318 Scientists: Persistent near-tropical warmth on the Antarctic continent during the early Eocene
epoch, *Nature*, 488, 73–77, doi:10.1038/Nature11300, 2012.
- Östlund, H.G., Craig, C. Broecker, W.S., and Spencer, D.: GEOSECS Atlantic, Pacific and Indian Ocean Expeditions: Shore
560 Based Data and Graphics, GEOSECS Atlas Ser., vol 7, 200 pp. U.S. Gov. Print. Off. Washington, D.C., 1987.
- Penman, D.E., and Zachos, J.C.: New constraints on massive carbon release and recovery processes during the Paleocene–
Eocene Thermal Maximum, *Environmental Research Letters*, 13(10), <https://doi.org/10.1088/1748-9326/aae285>, 2018.
- Penman, D.E., Keller, A., D'haenens, S., Kirtland Turner, S., and Hull, P.M.: Atlantic deep-sea cherts associated with Eocene
hyperthermal events, *Paleoceanography and Paleoclimatology*, 34, 287–299, <https://doi.org/10.1029/2018PA003503>,
565 2019.
- Quan, C., Liu, Y.-S.C., Utescher, T.: Paleogene evolution of precipitation in northeast China supporting the middle Eocene
intensification of the East Asian monsoon, *Palaios* 26, 743–753, 2011.
- Rau, G.H., Takahashi, T., Des Marais, D.J., Sullivan, C.W.: Particulate organic matter $\delta^{13}\text{C}$ variations across the Drake
Passage, *Geophys. Res. Oceans*, 96(C8), 15131–15135, <https://doi.org/10.1029/91JC01253>, 1991.
- 570 Röhl, U., Westerhold, T., Bralower, T.J., and Zachos, J.C.: On the duration of the Paleocene-Eocene thermal maximum
(PETM), *Geochem. Geophys. Geosyst.* 8 (12), Q12002, doi:10.1029/2007GC001784, 2007.
- Schmidtke, S., Stramma, L. and Visbeck, M.: Decline in global oceanic oxygen content during the past five decades, *Nature*,
542, 335–339, 2017.



- 575 Schmitz, B., and Pujalte, V.: Abrupt increase in seasonal extreme precipitation at the Paleocene-Eocene boundary, *Geology*, 35, 215-218, 2007.
- Sexton, P. F., Wilson, P. A., and Norris, R. D.: Testing the Cenozoic multisite composite δ 18O and δ 13C curves: New monospecific Eocene records from a single locality, Demerara Rise (Ocean Drilling Program Leg 207), *Paleoceanography*, 21(2), <https://doi.org/10.1029/2005PA001253>, 2006.
- 580 Shellito, C. J., Lamarque J.-F., and Sloan, L.C., Early Eocene Arctic climate sensitivity to pCO₂ and basin geography. *Geophys. Res. Lett.*, 36, L09707, doi:10.1029/2009GL037248, 2009.
- Sijp, W. P., England, M. H., and Toggweiler, J. R.: Effect of ocean gateway changes under greenhouse warmth, *Journal of Climate*, 22(24), 6639–6652. <https://doi.org/10.1175/2009JCLI3003>, 2009.
- 585 Sluijs, A., Brinkhuis, H., Schouten, S., Bohaty, S.M., John, C.M., Zachos, J.C., Reichart, G., Sinninghe Damste, J.S., Crouch E.M., and Dickens G.R.: Environmental precursors to rapid light carbon injection at the Paleocene/Eocene boundary, *Nature*, 450, 1218–1221, 2007.
- Sluijs, A., Bijl, P. K., Schouten, S., Rohl, U., Reichart, G. J., and Brinkhuis, H.: Southern ocean warming, sea level and hydrological change during the Paleocene-Eocene thermal maximum, *Clim. Past*, 7, 47–61, doi:10.5194/Cp-7-47-2011, 2011.
- 590 Sunderlin, D., Loope, G., Parker, N. E., and Williams, C. J.: Paleoclimatic and paleoecological implications of a Paleocene–Eocene fossil leaf assemblage, Chickaloon Formation, Alaska, *Palaios*, 26, 335–345, doi:10.2110/palo.2010.p10-077r, 2011.
- Tachikawa, K., Jeandel, C., and Roy-Barman, M.: A new approach to the Nd residence time in the ocean: the role of atmospheric inputs, *Earth Planet. Sci. Lett.* 170, 433–446, 1999.
- 595 Thomas, D.J.: Evidence for deep-water production in the North Pacific Ocean during the early Cenozoic warm interval, *Nature*, 430(6995), 65–68. <https://doi.org/10.1038/nature02639>, 2004.
- Thomas, D.J., Bralower, T.J., and Jones, C.E.: Neodymium isotopic reconstruction of late Paleocene–early Eocene thermohaline circulation, *Earth and Planetary Science Letters*, 209(3–4), 309–322. [https://doi.org/10.1016/S0012-821X\(03\)00096-7](https://doi.org/10.1016/S0012-821X(03)00096-7), 2003.
- 600 Thomas, E.: Cenozoic mass extinctions in the deep sea: What perturbs the largest habitat on Earth? *Geol. Soc. Am. Spec. Pap.*, 424, 1-23, 2007.
- Thomas, E., and Shackleton, N.J.: The Paleocene-Eocene benthic foraminiferal extinction and stable isotope anomalies, In: R.W.O.B. Knox, R. Corfield, R.E. Dunay (Eds.): *Correlation of the Early Paleogene in Northwest Europe*, *Geol. Soc. Spec. Pub.* 101, London, 401-441, 1996.
- 605 Toumoulin, A., Donnadieu, Y., Ladant, J.-B., Batenburg, S. J., Poblete, F., and Dupont-Nivet, G.: Quantifying the effect of the Drake Passage opening on the Eocene Ocean, *Paleoceanography and Paleoclimatology*, 35, e2020PA003889. <https://doi.org/10.1029/2020PA003889>, 2020.
- Via, R. K., and Thomas, D. J., 2006. Evolution of Atlantic thermohaline circulation: Early Oligocene onset of deep-water production in the North Atlantic, *Geology*, 34(6), 441. <https://doi.org/10.1130/G22545.1>
- 610 Wang, Q., Ferguson, D.K., Feng, G.-P., Ablav, A.G. e, Wang, Y-F., Yang, J., Li, Y.-L., Li, C.-S.: Climatic change during the Palaeocene to Eocene based on fossil plants from Fushun, China, *Palaeogeogr., Palaeoclim., Palaeoec.*, 295 (2010) 323-331.
- Wang, D., Lu, S., Han, S., Sun, X., and Quan, C.: Eocene prevalence of monsoon-like climate over eastern China reflected by hydrological dynamics, *J. Asian Earth Sci.*, 62, 776–787, doi:10.1016/j.jseaes.2012.11.032, 2013.
- 615 Westerhold, T., Röhl, U., Donner, B., McCarren, H. K., Zachos, J. C.: A complete high-resolution Paleocene benthic stable isotope record for the central Pacific (ODP Site 1209), *Paleoceanography*, 26, PA2216, doi:10.1029/2010PA002092.
- Wilf, P.: Late Paleocene–Early Eocene climate changes in southwestern Wyoming: paleobotanical analysis, *Geol. Soc. Am. Bull.*, 112, 292–307, doi:10.1130/0016-7606(2000)112<0292:Lpeecc> ,2.3.Co;2, 2000.
- Wilf, P., Wing, S. L., Greenwood, D. R., and Greenwood, C.L.: Using fossil leaves as paleoprecipitation indicators: an Eocene example, *Geology*, 26, 203–206, doi:10.1130/0091-7613(1998)026< 0203:UFLAPI> , 2.3.Co;2, 1998.
- 620 Wilf, P., Johnson, K. R., Cuneo, N. R., Smith, M. E., Singer, B. S., and Gandolfo, M. A.: Eocene plant diversity at Laguna del Hunco and Rio Pichileufu, Patagonia, Argentina, *Am. Nat.*, 165, 634-650, doi:10.1086/430055, 2005.



- Wing, S.L., and Greenwood, D.R.: Fossils and fossil climate: The case for equable continental interiors in the Eocene, *Phil. Trans.: Biol. Sci.*, 143 (1297), Paleoclimates and their Modelling with Special Reference to the Mesozoic Era, 243-252, 1993.
- 625 Wing, S. L., Harrington, G. J., Smith, F. A., Bloch, J. I., Boyer, D.M., and Freeman, K. H.: Transient floral change and rapid global warming at the Paleocene–Eocene boundary, *Science*, 310, 993-996, doi:10.1126/science.1116913, 2005.
- Winguth, A.M.E., Archer, D., Maier-Reimer, E. Mikolajewicz, U., and Duplessy, J.-C.: Sensitivity of paleonutrient tracer distribution and deep-sea circulation to glacial boundary conditions, *Paleoceanography*, 14, 304-323, 1999.
- Winguth A., Shellito, C., Shields, C., and Winguth C.: Climate response at the Paleocene-Eocene Thermal Maximum to greenhouse gas forcing – A model study with CCSM3. *Journal of Climate*, 23, 2562-2584, 2010.
- 630 Winguth, A.M.E., Thomas, E., and Winguth, C.: Global decline in ocean ventilation, oxygenation and productivity during the Paleocene-Eocene Thermal Maximum – Implications for the benthic extinction. *Geology*, 40, 263-266, doi:10.1130/G32529.1, 2012.
- Zacke, A., Voigt, S., Joachimski, M. M., Gale, A. S., Ward, D. J., and Tutken, T.: Surface-water freshening and high-latitude river discharge in the Eocene North Sea, *J. Geol. Soc. London*, 166, 969–980, doi:10.1144/0016-76492008-068, 2009.
- 635 Zachos, J.C., et al.: Rapid acidification of the ocean during the Paleocene-Eocene thermal maximum. *Science*, 308, 1611-1615, 2005.
- Zachos, J.C., Murphy, B., McCarren, H., Thomas, E., and Röhl, U.: A high-resolution record of the Elmo Event from Shatsky Rise, IODP Leg 198, Meeting on Climate and Biota of the Early Paleogene (CBEP), Bilbao, Spain, p. 151., 2006.
- 640 Zachos, J.C., Dickens, G. and Zeebe, R.: An early Cenozoic perspective on greenhouse warming and carbon-cycle dynamics. *Nature* 451, 279–283 <https://doi.org/10.1038/nature06588>, 2008.
- Zeebe, R.E., and Zachos, J.C.: Reversed deep-sea carbonate ion basin gradient during Paleocene-Eocene Thermal Maximum, *Paleoceanography*, 22, PA3201, <https://doi.org/10.1029/2006PA001395>, 2007.
- Zhang, Z.-S., Yan, Q., and Wang, H.: Has the Drake Passage played an essential role in the Cenozoic cooling? *Atmospheric and Oceanic Science Letters*, 3(5), 288–292. <https://doi.org/10.1080/16742834.2010.11446884>, 2010.
- 645 Zhang, Y., de Boer, A. M., Lunt, D.J., Hutchinson, D. K., Ross, P., van de Flierdt, T., et al.: Early Eocene ocean meridional overturning circulation: The roles of atmospheric forcing and strait geometry, *Paleoceanography and Paleoclimatology*, 37, e2021PA004329, <https://doi.org/10.1029/2021PA004329>, 2022.
- Zhu, J., Poulsen, C. J., and Tierney, J. E.: Simulation of Eocene extreme warmth and high climate sensitivity through cloud feedbacks, *Science Advances*, 5, eaax1874, <https://doi.org/10.1126/sciadv.aax1874>, 2019.
- 650 Zhu, J., and Poulsen, C.J.: Last Glacial Maximum (LGM) climate forcing and ocean dynamical feedback and their implications for estimating climate sensitivity, *Clim. Past*, 17, 253–267, <https://doi.org/10.5194/cp-17-253-2021>, 2021.